Cell

Article

Atomic Structure of the Cystic Fibrosis Transmembrane Conductance Regulator

Graphical Abstract

The positions of cystic fibrosis-causing missense mutations

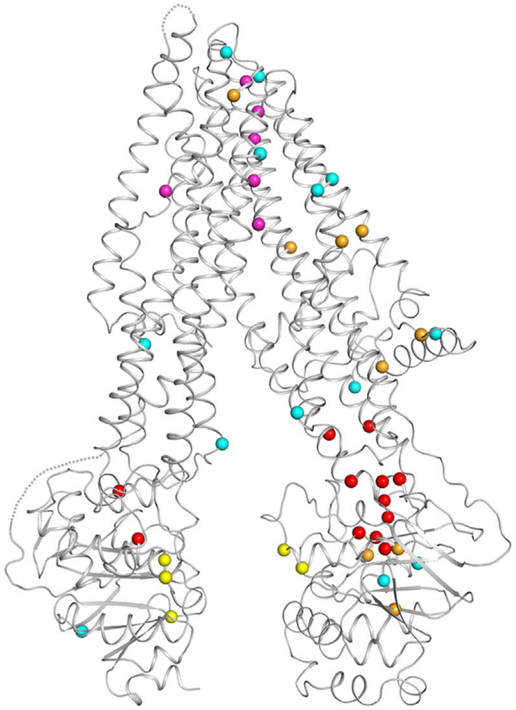

Authors

Zhe Zhang, Jue Chen

Correspondence

juechen@rockefeller.edu

In Brief

The atomic structure of CFTR provides a roadmap to a molecular understanding of cystic fibrosis.

Highlights

- Atomic structure of CFTR
- Funnel-shaped ion conduction pathway
- Asymmetrical opening of the nucleotide-binding domains
- Structural interpretation of cystic fibrosis-causative mutations

Data Resources

5TSI

Zhang & Chen, 2016, Cell *167*, 1586–1597
December 1, 2016 © 2016 Elsevier Inc.
http://dx.doi.org/10.1016/j.cell.2016.11.014

Cell

Article

Atomic Structure of the Cystic Fibrosis Transmembrane Conductance Regulator

Zhe Zhang[1] and Jue Chen[1,2,*]
[1]The Rockefeller University and Howard Hughes Medical Institute, 1230 York Avenue, New York, NY 10065, USA
[2]Lead Contact
*Correspondence: juechen@rockefeller.edu

http://dx.doi.org/10.1016/j.cell.2016.11.014

SUMMARY

The cystic fibrosis transmembrane conductance regulator (CFTR) is an anion channel evolved from the ATP-binding cassette (ABC) transporter family. In this study, we determined the structure of zebrafish CFTR in the absence of ATP by electron cryo-microscopy to 3.7 Å resolution. Human and zebrafish CFTR share 55% sequence identity, and 42 of the 46 cystic-fibrosis-causing missense mutational sites are identical. In CFTR, we observe a large anion conduction pathway lined by numerous positively charged residues. A single gate near the extracellular surface closes the channel. The regulatory domain, dephosphorylated, is located in the intracellular opening between the two nucleotide-binding domains (NBDs), preventing NBD dimerization and channel opening. The structure also reveals why many cystic-fibrosis-causing mutations would lead to defects either in folding, ion conduction, or gating and suggests new avenues for therapeutic intervention.

INTRODUCTION

The cystic fibrosis transmembrane conductance regulator (CFTR) is a compelling molecule to study both for its biomedical importance and its unique functional properties. Mutation of the *CFTR* gene causes cystic fibrosis (CF), a lethal disease with a prevalence of 1 in 2,500 in Caucasian populations (Boat et al., 1989; Rommens et al., 1989). Sequencing information from 88,664 patients has now identified a total of 272 mutations that cause cystic fibrosis (http://cftr2.org/). Some mutations cause defective CFTR biosynthesis, resulting in diminished or absent protein production. Others are missense mutations that produce misfolded or dysfunctional protein. Lack of functional CFTR in epithelial tissues disrupts salt homeostasis of the lung, intestine, pancreas, and kidney. The most serious consequence is impaired mucus clearance of the airway, which leads to recurrent infections, chronic inflammation, and eventual respiratory failure (Elborn, 2016).

CFTR belongs to the large family of the ATP-binding cassette (ABC) transporters. Among the thousands of ABC transporters identified from bacteria to human, CFTR is the only member of the family known to function as an ATP-gated ion channel. All other ABC transporters are active pumps that utilize the free energy from ATP hydrolysis to concentrate substrates across the biological membrane (Theodoulou and Kerr, 2015). Structurally, CFTR is similar to other ABC transporters: it contains two transmembrane domains (TMDs) that form the anion conduction pathway and two cytoplasmic nucleotide-binding domains (NBDs) that bind and hydrolyze ATP. A large regulatory (R) domain, unique to CFTR, connects the two halves of the protein and plays an essential role in regulating the channel activity (Riordan, 1993).

Unlike other ligand-gated ion channels, CFTR is not regulated by changes in the concentration of its ligand. Both phosphorylation of the R domain and ATP binding to the NBDs are required to open the CFTR channel (Cheng et al., 1991). As the intracellular concentration of ATP is near saturating and relatively constant, the activity of CFTR is predominantly regulated by cyclic AMP/protein kinase A (PKA)-dependent phosphorylation (Frizzell and Hanrahan, 2012). Furthermore, CFTR consumes the ligand by catalyzing ATP hydrolysis. Similar to other ABC transporters, two ATPase sites are located at the interface of a closed NBD dimer. In CFTR, only one ATPase site is catalytically competent. The other site, which contains non-consensus residues, including the Walker B motif of NBD1 and the ABC signature motif of NBD2, is deficient in ATP hydrolysis (Aleksandrov et al., 2002; Basso et al., 2003).

In this study, we determined the structure of the zebrafish CFTR by electron cryo-microscopy (cryo-EM) to 3.7 Å resolution. Similar to human CFTR, zebrafish CFTR plays an essential role in regulating fluid homeostasis (Bagnat et al., 2010). The loss of CFTR function in zebrafish leads to pancreatic destruction, a pathology similar to pancreatic insufficient cystic fibrosis in humans (Navis and Bagnat, 2015). Interpreted in light of the vast set of functional data on human CFTR, the cryo-EM structure provides a new molecular understanding of this important molecule.

RESULTS AND DISCUSSION

Biochemical Characterization

Zebrafish CFTR, which shares 55% overall sequence identity to human CFTR (Figure S1), is stable in detergent micelles and could be purified to homogeneity in large scale (Figure 1A). To test whether the protein functions after our expression and purification procedure, we measured the ATPase activities of the purified sample in both fully dephosphorylated and phosphorylated states (Figure 1B). As expected for CFTR, phosphorylation

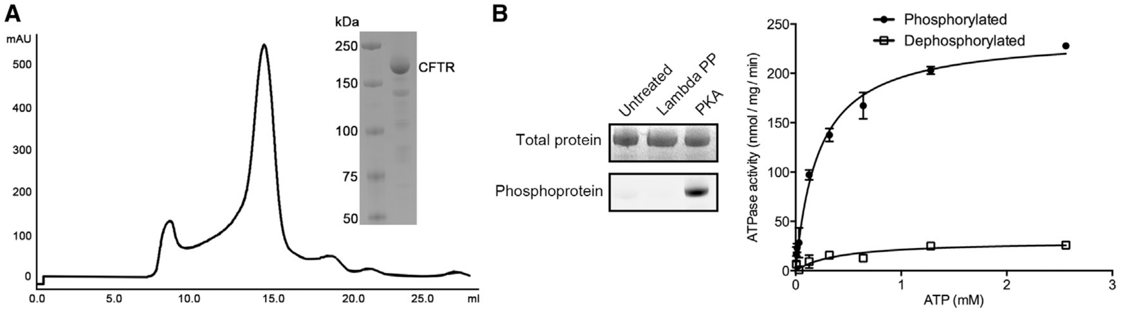

Figure 1. Biochemical Properties of Zebrafish CFTR

(A) Size exclusion profile and SDS-PAGE of the purified sample.

(B) Phosphorylation stimulates the ATPase activity of CFTR. Left: the phosphorylation state of the untreated, lambda protein phosphatase (PP)-treated, and PKA-treated samples stained by Coomassie blue (upper) and the Pro-Q Diamond Phosphoprotein Gel Stain (lower). Right: ATPase activity as a function of ATP concentration. Data points represent the means and SEs of three measurements. At 28°C, the PKA-treated phosphorylated protein shows a K_M of 0.22 ± 0.02 mM for ATP. The maximal ATPase activity is determined to be 239 ± 6 nmol/mg/min (assuming a molecular weight of 168 kDa, the specific ATP turnover rate is 0.66 per second). For dephosphorylated sample, K_M is 0.4 ± 0.2 mM and the maximal activity is 30 ± 5 nmol/mg/min (or 0.08 per second).

stimulated the maximal ATPase activity by 8-fold. Phosphorylated zebrafish CFTR has a K_M of 0.22 mM for ATP, comparable to the 0.30 mM value reported for human CFTR (Li et al., 1996). The ATPase activity at near-saturating ATP concentrations (i.e., maximal) for human CFTR was reported to be in the range of 125–250 nmol/mg/min, corresponding to a specific turnover rate of 0.5–1.0 per second (Li et al., 1996). Our measured ATPase activity at near saturating ATP concentration for zebrafish CFTR is 239 ± 6 nmol/mg/min, corresponding to a specific turnover rate of 0.66 per second—very close to the estimate for human CFTR. Independently, single channel recordings on human CFTR have provided an estimate of the true gating cycle rate, which is 0.45 per second (Vergani et al., 2003). This value is very close to our specific ATP turnover rate. The significance of this correlation is that it implies that 100% of the CFTR protein in our preparation is active.

Structure Determination

As the first step to reveal the structures of CFTR in a gating cycle, we determined the structure of the dephosphorylated protein in the absence of ATP by single molecule cryo-EM. This structure represents the ATPase downregulated, channel-closed conformation. The overall resolution of the structure is estimated to be 3.7 Å (Figure S2; Table S1). The EM density exhibits prominent side-chain features in the TM region that allow us to unambiguously identify the amino acid register for all 12 TM helices (Figures 2 and S3). The densities corresponding to the NBDs are not as sharply resolved (Figure S3); we relied on the crystal structures of mouse NBD1 and human NBD2 (PDB: 1Q3H and 3GD7, respectively) to guide model building. Density for the R domain is too weak to assign secondary structure, however, its location is clearly visible. The final model, containing residues 1–1,437, except for 171 residues in the R domain and a few loop regions, was refined against the EM density to excellent geometry and statistics (Table S1).

The overall structure of CFTR resembles a typical ABC transporter in the inward-facing conformation (Figures 3A and 3B). The two TMDs are domain-swapped such that TM 4-5 and TM 10-11 reach across the interface to pack against the other half of the molecule. The two cytosolic NBDs are separated with the mostly unstructured R domain wedged in between. It also contains an N-terminal interfacial structure never before seen in any of the ABC transporters, which we refer to as the lasso motif.

The zebrafish CFTR structure is compatible with the extensive crosslinking data obtained from human CFTR (Gao and Hwang, 2016; He et al., 2008; Serohijos et al., 2008; Wang et al., 2011; Wang and Linsdell, 2012; Zhou et al., 2010). A few examples, representing different regions of the protein, are shown in Figure 3C, where pairs of residues shown to crosslink by cysteine mutagenesis are located in close proximity to each other. Furthermore, as we will discuss in detail, the structures of the ion conduction pathway and the extracellular gate are entirely compatible with a large body of functional data from studies of human CFTR. Thus, we are confident that the structure of zebrafish CFTR is an excellent model with which to interpret decades of biochemical and functional studies on this important protein. For ease of understanding, individual residues discussed in this work are highlighted in the sequence alignment (Figure S1) and numbered according to the human CFTR sequence.

The Regulatory Domain

The R domain contains ~200 residues, including more than ten potential phosphorylation sites (Seibert et al., 1999). Co-expression of the two halves of CFTR devoid of the R domain results in an ATP-gated channel independent of phosphorylation (Csanády et al., 2000). The opening rates of the split channel are similar to those of the phosphorylated wild-type protein, suggesting that in the dephosphorylated state the R domain inhibits channel opening and such inhibition is liberated upon phosphorylation (Csanády et al., 2000).

The N-proximal end of the R domain (residues 654–669) forms a helix, as observed in the crystal structure of the isolated NBD1 (Lewis et al., 2004). In addition, the EM map at a lower contour exhibits densities for the detergent micelles as well as some

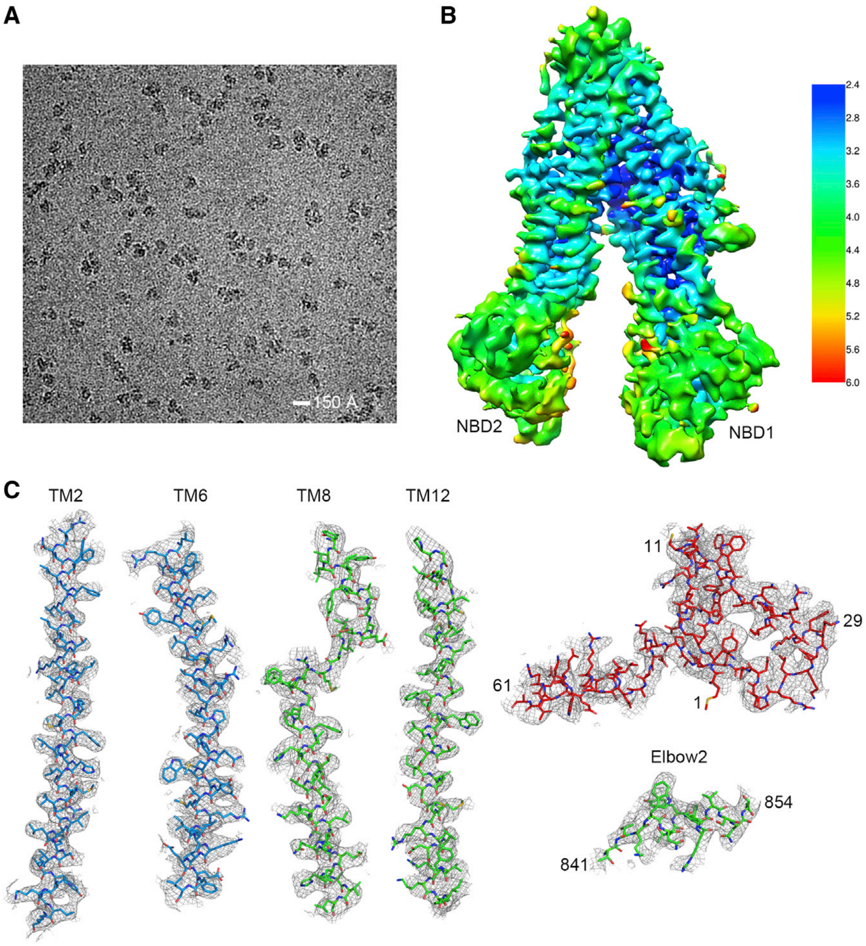

Figure 2. Cryo-EM Studies of CFTR

(A) A representative EM micrograph at defocus −2.4 μm.

(B) Density map colored by local resolution estimation using blocres (Heymann and Belnap, 2007).

(C) Representative EM densities at various regions.

See also Figures S1, S2, and S3 and Table S1.

amorphous density that lies in between NBD1 and the elbow helix of TMD2, likely contributed by the remainder of the R domain and the regulatory (R) insertion loop in NBD1 (Figures 3B and S4). Biochemical and NMR studies of the isolated R domain (Baker et al., 2007; Ostedgaard et al., 2000) and the crystal structure of NBD1 (Lewis et al., 2004) indicate that both regions are largely unstructured. Here, we show that in the context of the full-length CFTR, the R domain and the R insertion are flexible. The general location of the R domain between the two halves of the molecule suggests that it would prevent the formation of the closed ATP-bound NBD dimer, consistent with its inhibitory role in the unphosphorylated state (Csanády et al., 2000; Ma et al., 1997; Winter and Welsh, 1997).

A Novel Interfacial Motif

CFTR as well as other members the ABCC subfamily, including the multidrug-resistant proteins (MRP1–MRP9) and two sulfonylurea receptors (SUR 1 and 2), contain a cytosolic region of ∼60 residues preceding the elbow helix 1 (Figure S5). We call this region the "lasso motif" because of its shape: the first 40 residues, which are partially inserted into the membrane, form a circular noose packed against TM 10-11 (Figures 2C and 4A). The extended end of the lasso, residues 46–61, form the lasso helix 2 (Lh2), which is tucked under the elbow helix 1. It was reported that a single-alanine substitution of four acidic residues in the lasso motif reduces the steady-state currents of CFTR (Naren et al., 1999). These residues are located in Lh2 facing away from the membrane bilayer (Figure 4A).

The importance of the lasso motif is underscored by several mutations in this region that cause cystic fibrosis (Table S2). It is known that the lasso motif interacts with the membrane traffic machinery (Naren et al., 1998; Peters et al., 2001) and mutations in this region cause intracellular retention or abnormal gating (Bilan et al., 2004; Fu et al., 2001; Gené et al., 2008; Jurkuvenaite et al., 2006; Naren et al., 1998, 1999; Peters et al., 2001; Prince et al., 1999). It has also been postulated that the lasso motif regulates the channel gating through interactions with the R domain (Fu et al., 2001; Naren et al., 1999). The lasso motif is located in the vicinity of the density corresponding to the R domain, but no direct contact is observed in this closed-channel conformation (Figures 3B and 4A).

Asymmetric Opening of the NBDs

One intensely debated mechanistic question is whether and how far the two NBDs separate during the gating cycle (Chaves and Gadsby, 2015; Csanády et al., 2013; Szollosi et al., 2011; Tsai et al., 2010). Different structures of ABC exporters captured in the inward-facing conformation by X-ray crystallography and EM display various degrees of separation between the NBDs (Locher, 2016). Whether a large opening of the NBD interface occurs at physiological ATP levels has been questioned (Perez et al., 2015). Indeed, as CFTR contains only a single catalytically competent site for ATP hydrolysis, it has been suggested that the NBDs of CFTR remains in contact at the degenerate site even in the closed-channel conformation (Szollosi et al., 2011; Tsai et al., 2010). However, recent accessibility analysis demonstrates that upon channel closure, the two NBDs rapidly separate to a distance between 8 and 45 Å at both sites (Chaves and Gadsby, 2015).

In this study, we aligned projections of 0.8 million molecules to generate the 3D structure of the ATP-free, dephosphorylated CFTR. Analysis of structural heterogeneity by means of 3D classification did not reveal structures that are significantly different

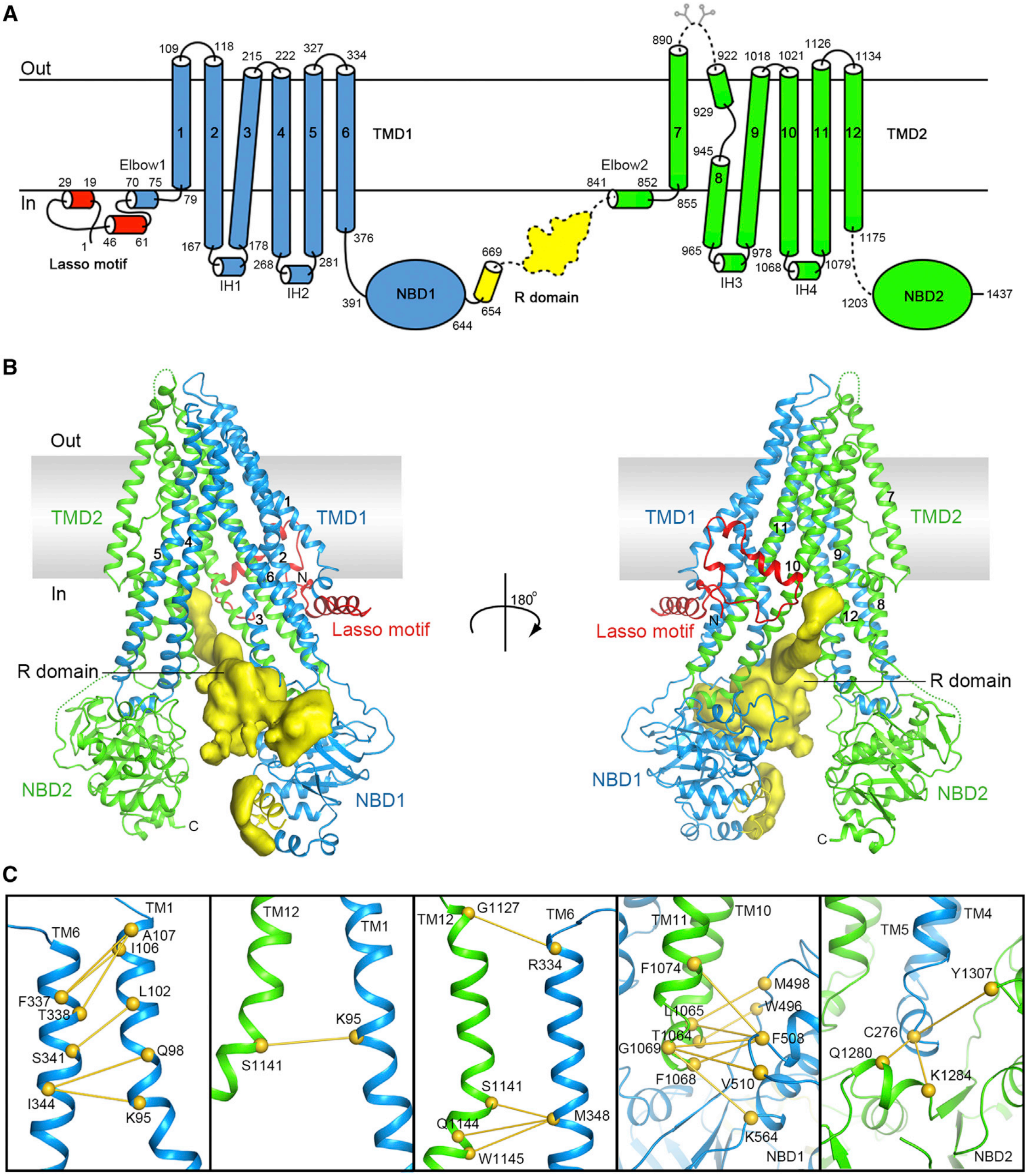

Figure 3. The Overall Structure

(A) The domain structure of CFTR.

(B) Ribbon diagram of the TMDs and NBDs. Also shown is the EM density corresponding to the R domain.

(C) Pairs of residues in human CFTR that were crosslinked (gold lines) when mutated to cysteines (Gao and Hwang, 2016; He et al., 2008; Serohijos et al., 2008; Wang et al., 2011; Wang and Linsdell, 2012; Zhou et al., 2010).

See also Figures S1 and S4.

from each other. All 0.8 million particles were used to calculate the final reconstruction, which reveals an open NBD interface entirely consistent with the accessibility studies of functioning channels in the membrane (Figure 4B) (Chaves and Gadsby, 2015). Furthermore, the cryo-EM structure reveals an asymmetric feature that is unique to CFTR: the Walker A and the signature motifs of the catalytically competent site are closer to each other than those of the degenerate site (Figure 4B). The distance between the Cα atoms of the conserved glycine residue in the Walker A motif and the serine residue in the signature motif is 17 Å in the competent site, compared to 27 Å in the degenerate site (Figure 4B). This asymmetric opening at the NBD

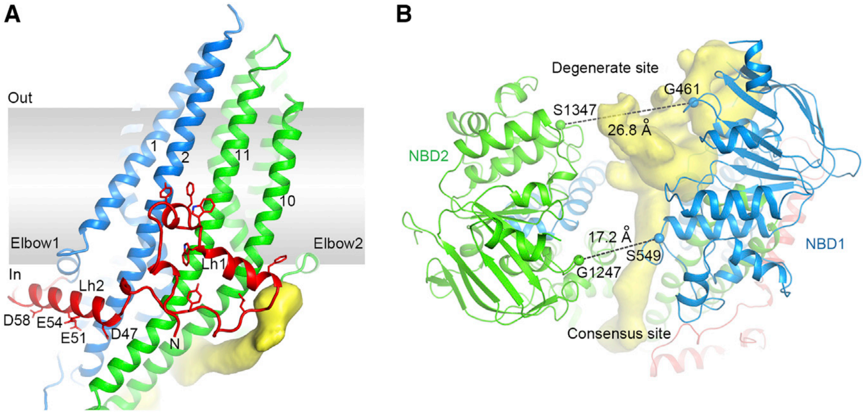

Figure 4. Two Unique Features of CFTR

(A) The N-terminal lasso motif (red). Lh1 and Lh2: lasso helix 1 and 2. TM 1 and 2 are shown in blue, TM 10 and 11 in green. Density corresponding to the R domain is shown in yellow.

(B) The asymmetric opening of the NBD interface. The distances between equivalent residues in the two ATPase sites are indicated.

See also Figure S5 and Table S2.

interface is caused by the presence of the R domain, which inserts between the two halves of the protein on the side of the degenerate site (Figures 3B and 4B). Access to the NBD1 Walker A motif is partially blocked by the R domain, indicating that ATP binding to the degenerate site would be obstructed by the unphosphorylated R domain.

For a typical ABC transporter, ATP binding to the completely separated NBDs is insufficient to promote a global conformational change. Substrate binding stabilizes a pre-translocation conformation, in which the Walker A motifs are brought closer to the NBD dimer interface (Oldham and Chen, 2011). For CFTR, it is likely that phosphorylation activates the ATPase activity by releasing the R domain from the intracellular opening. ATP binding to the phosphorylated conformation or to channels lacking the R domain would promote progression to an open-channel conformation.

The Ion Conduction Pathway

Previously, functional studies exploiting the substituted cysteine accessibility method (SCAM), crosslinking, whole-cell, and single-channel current recording methods have identified a large number of residues whose modification influences anion conduction (reviewed in El Hiani and Linsdell, 2014). By analyzing these functional data with the structure, a plausible route for ion conduction can be deduced.

In the structure, we observe a large vestibule at the interface of the TMDs that opens to the cytosol only on one side of the molecule, between TM 4 and 6 (Figure 5A). A cytosolic opening between TM 10 and 12 is often observed in other ABC transporters, but in CFTR this space is filled by the R domain (Figures 3B and 5A). The single lateral opening is consistent with recent data showing that while mutation and covalent modification of positively charged residues in the intracellular extensions of TM 4 and 6 strongly impacted the Cl^- permeation rate, modification of equivalent positions in TM 10 and 12 had a lesser effect (El Hiani and Linsdell, 2015; Linsdell, 2016b). Approximately halfway into the lipid bilayer, the vestibule tapers down to a narrow tunnel extending to just below the extracellular surface of the membrane (Figure 5A). The electrostatic surfaces of the vestibule and this tunnel are highly positive (Figure 5B) and lined by polar and charged residues, many of which have been functionally characterized to interact with anions including K95, Q98, E267, R303, S341, R352, and K1060 (Anderson et al., 1991; Aubin and Linsdell, 2006; Bai et al., 2010; Billet et al., 2013; Gao et al., 2013; Guinamard and Akabas, 1999; Linsdell, 2005; McDonough et al., 1994; Wang et al., 2011; Zhou et al., 2010).

The discontinuity of helix TM8, which makes two sharp breaks inside the membrane, is a notable feature of CFTR (Figure 5A). The helical breaks free main-chain atoms from their secondary structure hydrogen bonds and render them available to interact with ions and water along the ion conduction pathway. The interaction of main-chain atoms with conducting ions is an important feature of some other ion channels as well (Doyle et al., 1998; Dutzler et al., 2002). Another potential functional consequence of breaks in helical secondary structure is that they can create flexible hinges to facilitate gating. Consistent with this latter hypothesis, a leucine-to-proline mutation in the TM8 loop (L927P) causes gating defects and leads to cystic fibrosis (Van Goor et al., 2014). In addition to these mechanistic ideas, we note that as a result of the unusual trajectory of TM8, helix TM7 is displaced from its usual position in ABC transporters and does not line the pore in CFTR, consistent with functional data (Wang et al., 2014a; Zhang and Hwang, 2015).

A constriction region, formed by residues at the extracellular ends of TM 1, 6, 8, and 12, blocks access from the exterior of the cell (Figure 6A). Among the residues forming this gate, mutations of F337 and T338 have been shown to disrupt anion conductance and ATP-dependent gating (Bai et al., 2010; Linsdell, 2001; Linsdell et al., 2000; Wei et al., 2016). A salt bridge between R347 and D924, previously identified by mutagenesis (Cotten and Welsh, 1999), lines the interior surface of the pore (Figure 6B). Disruption of this salt bridge destabilizes the conducting state of single CFTR channels (Cotten and Welsh, 1999); the mutations R347H and R347P lead to cystic fibrosis (Table S2). Here, we show that the R347-D924 salt bridge also plays a structural role in the closed-channel conformation. Another salt bridge, between residues R352 and D993, has also been identified to stabilize the open pore (Cui et al., 2008). In our channel-closed structure, these two residues are located in TM 6 and TM 9, respectively, oriented toward each other with a 15 Å separation between their atoms. It is possible that in the ATP-bound channel-open conformation TM6 is closer to TM9 to form the R352-D993 salt bridge.

The structure of the ion conduction pathway is also consistent with the large body of SCAM data aimed at mapping pore-lining

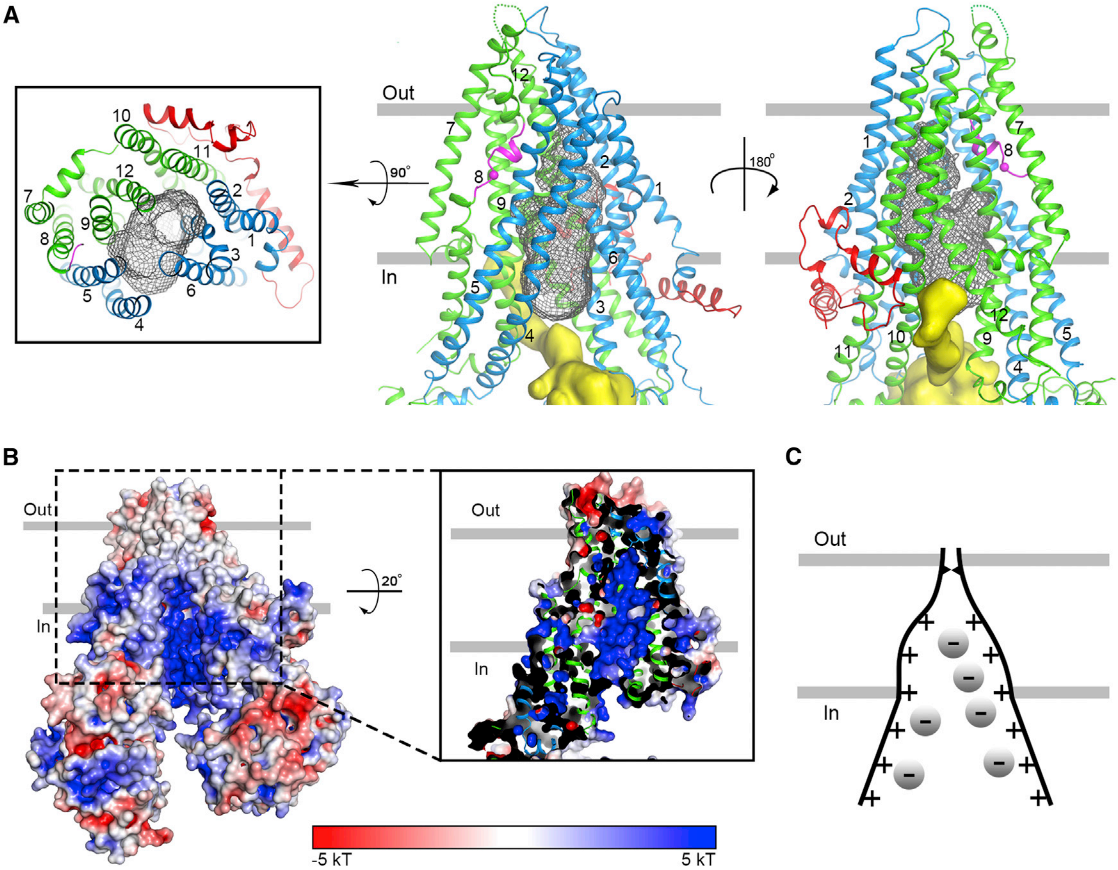

Figure 5. The Ion Conduction Pathway

(A) The pore, shown as a gray mesh, is defined by a probe with the size of a dehydrated chloride ion (1.7 Å radius). The extended helix-breaking loop in TM 8 is highlighted in magenta. The location of the CF-causing mutation L927P is indicated by a sphere. A cross-section at the center of the membrane is showed on the left.

(B) The electrostatic property of the interior surface of the pore, calculated at pH 7 and 0.15 M concentrations of both (+1) and (−1) ions.

(C) A schematic drawing of the funnel-shaped ion permeation pathway.

residues (Alexander et al., 2009; Bai et al., 2010, 2011; Beck et al., 2008; El Hiani and Linsdell, 2010; Gao et al., 2013; Qian et al., 2011; Wang et al., 2011, 2014a; Zhang and Hwang, 2015). In these studies, cysteines were introduced individually to the TM helices and their accessibility to methane thiosulfonate (MTS) compounds or pseudohalide probes was analyzed. Figure 6C shows that with only one exception, residues found to be modified by cytoplasmic MTS reagents when channels were closed are located at the intracellular side of the gate (Figure 6C, orange). Residues modified by extracellular MTS but inaccessible from the cytosol are mostly located outside the membrane (Figure 6C, yellow). The proposed gating residues, which can be reached from both sides of the membrane (presumably depending on whether the channel is open or closed), or from the cytoplasmic side only when channels are activated, are indeed clustered around the constriction region (Figure 6C, magenta).

Based on this structure and available functional information, we establish that the ion conduction pathway is funnel shaped and consists of a large cytosolic vestibule leading to a narrow transmembrane tunnel (Figure 5C). Positively charged residues line the entire length of the funnel, contributing to anion selectivity and conduction. There is only a single gate in the channel, located near the extracellular ends of TM 1, 6, 8, and 12 (Figure 6A). Small displacements of these helices in the ATP-bound conformation could open the gate to form a larger ion conduction pathway penetrating the entire lipid bilayer. Remarkably, the configuration of a large cytosolic vestibule and an extracellular gate was already deduced from functional studies (Bai et al., 2010, 2011; Linsdell, 2016a; Smith et al., 1999). A further understanding of channel gating and selectivity will require the structure of an open channel.

Structural Interpretation of the Cystic-Fibrosis-Causative Mutations

The most recent analysis (http://CFTR2.org) has identified 53 missense CF-causing mutations that affect 46 positions in CFTR (Table S2). To gain a better mechanistic understanding of these potentially lethal mutations, we mapped these 46 sites onto the structure. By correlating the mutations with their functional consequences (reviewed in Veit et al., 2016 and

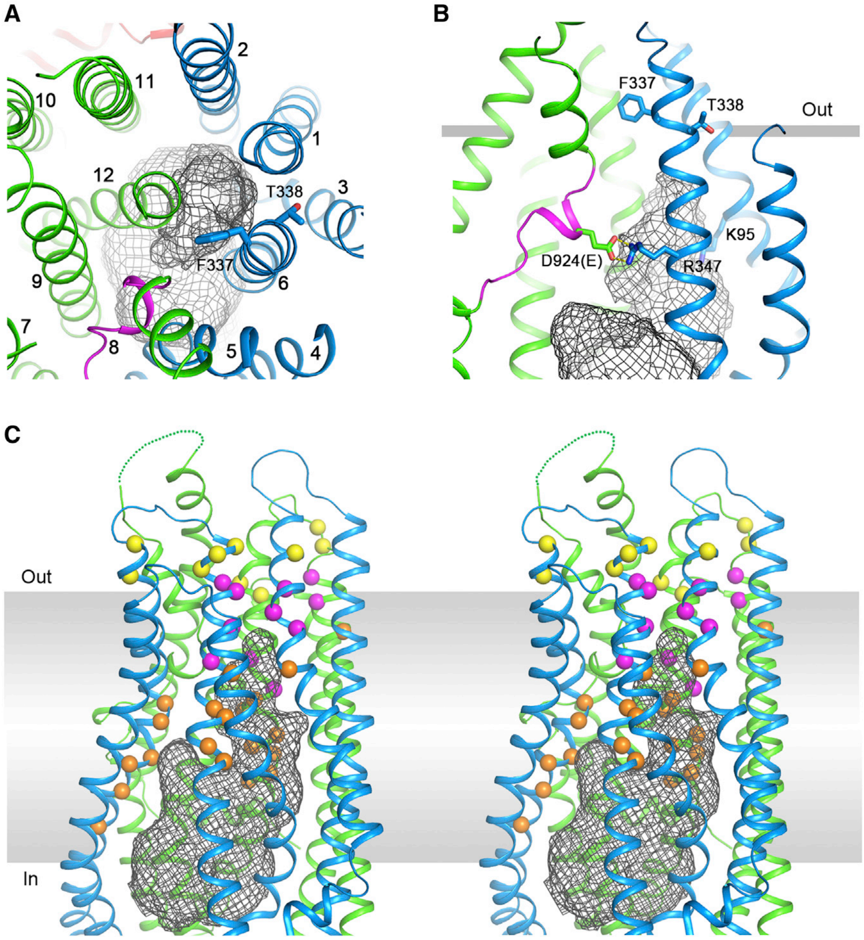

Figure 6. The Structure of the Pore Is Compatible with Functional Data

(A) The positions of two characterized gating residues, F337 and T338, viewed along the membrane normal from the extracellular side.

(B) Residues R347 and D924 (E in zebrafish) stabilize the pore by forming a salt bridge (Cotten and Welsh, 1999). The positions of the well-studied residues K95, F337, and T338 are also shown.

(C) Stereoview of the ion conduction pathway. Residues accessible to MTS regents from inside the cell are shown as orange spheres, including K95, A299, R303, N306, S307, F310, F311, V345, M348, A349, R352, Q353, I1112, S1141, T1142, Q1144, W1145, V1147, N1148, and S1149 (reviewed in El Hiani and Linsdell, 2014 and Zhang and Hwang, 2015). Residues accessible from outside the cell are shown in yellow, including R104, L323, A326, R334, K335, I336, T1121, T1122, I1131, and I1132 (reviewed in El Hiani and Linsdell, 2014 and Zhang and Hwang, 2015). The pore-constriction residues, Q98, P99, L102, F337, T338, S341, I344, T1115, S1118, N1138, and M1140, are shown in magenta (reviewed in El Hiani and Linsdell, 2014).

Wang et al., 2014b), we can describe them using four categories (Figure 7; Table S2).

Pore Construction Mutations

The pore construction mutations group includes amino acid substitutions expected to change the structure or the electrostatic environment of the pore (Figures 7A and 7B). Most of these mutations have been characterized functionally and shown to affect ion conduction (Table S2).

Folding Mutations

Many mutations involve substitution of a hydrophobic residue with a charged amino acid, introduction of a proline, or elimination of a glycine residue. These changes are likely to destabilize the structure of CFTR and cause folding defects. For example, two CF-causing mutations were found at the very site where TM1 comes into close contact with TM3 (Figure 7C). Both mutations, G85E and H199Y, would disrupt this observed interaction. The G85E mutant has indeed been shown to be defective in protein processing (Decaestecker et al., 2004; Van Goor et al., 2014). The H199Y mutant is likely to have a similar defect.

ATPase Site Mutations

Six mutations are found in the consensus ATPase site, including S549R, S549N, G551D, and G551S within the NBD1 signature sequence, and G1244E and S1251N in the NBD2 Walker A motif (Figure 7D). These mutated residues are important for ATP binding and/or hydrolysis and all have been shown to have deficits in channel gating (Bompadre et al., 2007; Yang et al., 1993; Yu et al., 2012). The degenerate ATPase site also contains a CF-causing mutation, G1349D, which introduces a negatively charged residue to the NBD2 signature sequence and results in diminished channel activity (Bompadre et al., 2007), likely by interfering with ATP binding and formation of the closed NBD dimer.

NBD/TMD Interface Mutations

Interactions between TMDs and NBDs maintain integrity of the structure and transmit conformational changes from the NBDs to the TMDs, thereby coupling phosphorylation and ATP hydrolysis to channel gating. It is therefore not surprising that mutations at these interfaces cause defects both in folding and gating. A large number of CF-causing mutations are found at the two NBD/TMD interfaces. Eleven of these mutations at eight sites are located either in IH4 or at the molecular surface of NBD1 where IH4 docks (Figure 7E), including S492F, ΔI507, ΔF508, R560K, R560S, R560T, A561E, G1061R, L1065P, R1066C, and R1066H. In addition, the H1054D and L1077P mutations are in close proximity to IH4 and are likely to disturb the structure of IH4. All of these mutants have been shown to be defective in protein processing or channel function (reviewed in Veit et al., 2016). The most prevalent mutation, the deletion of F508, is responsible for about 70% of all CF disease and results in intracellular retention and rapid degradation of the channel (Cheng et al., 1990). A small number of the ΔF508 mutants reach the plasma membrane, but are unstable and dysfunctional (Dalemans et al., 1991; Lukacs et al., 1993; Sharma et al., 2001). The side chain

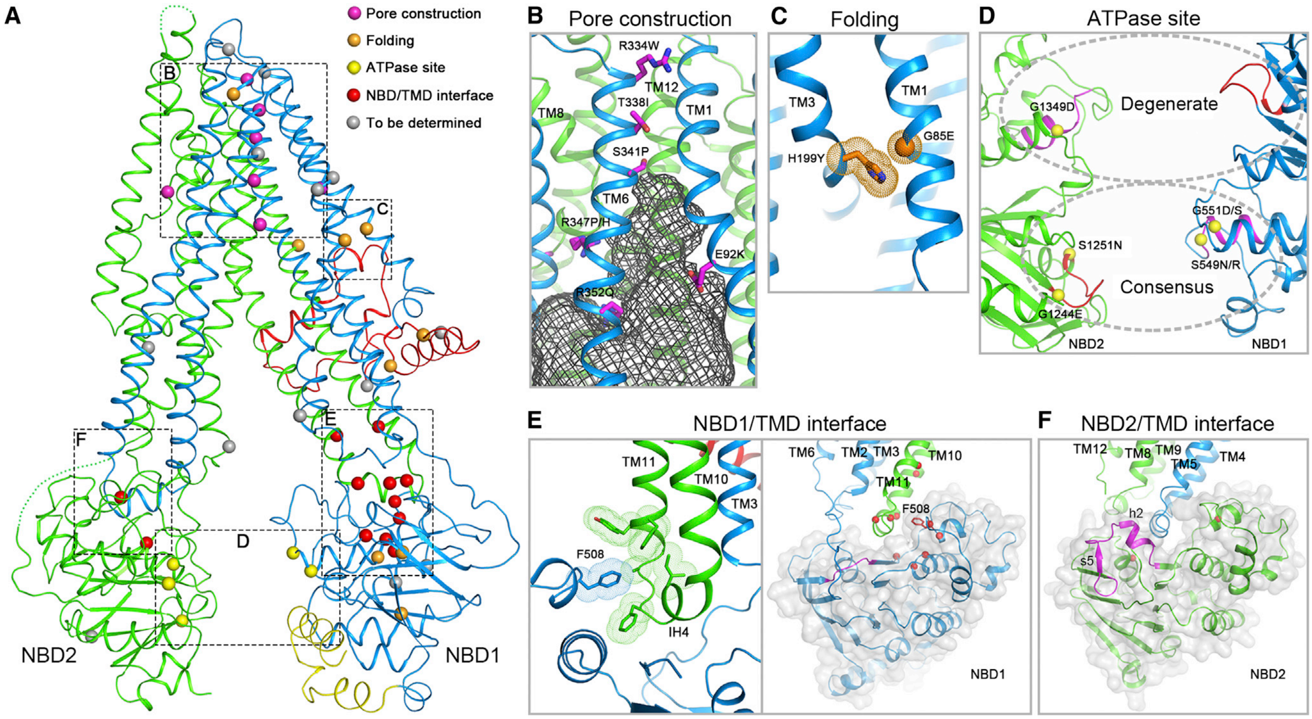

Figure 7. The Locations of CF-Causing Mutations

(A) The overall structure. The locations of (B–F) are indicated. Color code for mutations: magenta, pore construction; orange, folding; yellow, ATPase site; red, NBD/TMD interface; silver, structural consequences yet to be determined.

(B) Mutations that may disrupt the ion conduction pathway are indicated and shown in magenta sticks.

(C) Close packing of TM 1 and TM 3 at the site of two CF-causing mutations.

(D) Mutations in the Walker A (red) and the signature motifs (magenta) are indicated and shown as yellow spheres.

(E) The NBD1/TMD interface. Left: F508 stabilizes the interface through van der Waals interactions with residues in TM 11 and IH4. Right: NBD1 has a less extensive interface with the TMD compared to NBD2.

(F) The mutational sites are indicated as red spheres. The s5, h2 segments in NBD2 and the equivalent region in NBD1 are shown in magenta.

See also Table S2.

of F508 inserts into a hydrophobic pocket at the conjunction of IH4/TM11, making van der Waals interactions with residues from IH4 and TM 11 (Figure 7E). Although deletion of F508 has little effect on the overall conformation of NBD1 (Lewis et al., 2005), the structure clarifies how it would impair the assembly of the entire protein and thereby depletes cells of functional CFTR channels.

An intriguing observation is that the CF-causing mutations are unevenly distributed between the two NBD/TMD interfaces. Thirteen mutations are targeted to the NBD1/TMD interface, but only two (S1255P and N1303K) at the equivalent region where NBD2 interacts with IH2 (Figure 7). This can probably be explained by the structural differences between these two interfaces (Figures 7E and 7F). The TMD/NBD interfaces in all ABC transporters share a common structure that resembles a ball-and-socket joint. Each TMD is bound to an NBD through docking of a short intracellular helix (the "ball") onto a surface cleft on the NBD (the "socket") (Oldham et al., 2008). As previously discussed (Lewis et al., 2004), CFTR lacks a segment containing a β strand (s5) and an α helix (h2) in NBD1. Consequently, an important helical component of the socket (h2) is absent in NBD1, leading to a weaker contact with the TMD compared with the NBD2/TMD interface (Figures 7E and 7F). This unique feature of NBD1 makes the NBD1/IH4 interface particularly vulnerable to mutation. However, part of the NBD1/TMD interface is exposed to solvent due to this absence of the h2 helix, offering a potential target for rational drug design. Compounds that functionally mimic the h2 helix could possibly act as "folding correctors" (and perhaps "gating potentiators") to treat patients with mutations at this interface.

We note that no CF-causing mutation is located in the R domain. This implies that some phosphorylation sites must be functionally redundant, so that losing a single site by mutation would not abolish channel regulation. Moreover, it is also consistent with the inhibitory role of the unphosphorylated R domain. We reason that mutations are more likely to diminish than enhance the interactions of the R domain with the rest of the protein. Such mutations might decouple channel opening from phosphorylation, but would not abolish ATP-driven channel activity.

In summary, we present here the structure of CFTR in the dephosphorylated state in the absence of ATP. The overall architecture of CFTR underscores its evolutionary relationship with other ABC transporters. This structure, strongly supported by a large body of functional data, offers a fresh basis to understand human cystic fibrosis and facilitate drug development.

STAR★METHODS

Detailed methods are provided in the online version of this paper and include the following:

- KEY RESOURCES TABLE
- CONTACT FOR REAGENT AND RESOURCE SHARING
- EXPERIMENTAL MODEL AND SUBJECT DETAILS
  - ○ Cell Culture
- METHOD DETAILS
  - ○ Protein Expression and Purification
  - ○ ATPase Activity Assay
  - ○ EM Sample Preparation and Imaging
  - ○ Image Processing and 3D Reconstruction
  - ○ Model Building
  - ○ Model Refinement and Validation
- QUANTIFICATION AND STATISTICAL ANALYSIS
- DATA AND SOFTWARE AVAILABILITY
  - ○ Data Resources

SUPPLEMENTAL INFORMATION

Supplemental Information includes five figures and two tables and can be found with this article online at http://dx.doi.org/10.1016/j.cell.2016.11.014.

AUTHOR CONTRIBUTIONS

Z.Z. performed all the experiments. Z.Z. and J.C. analyzed the data and prepared the manuscript.

ACKNOWLEDGMENTS

We thank David Gadsby and Roderick MacKinnon for discussions and critical comments on the manuscript; Eric Gouaux for reagents of the mammalian expression system; Mark Ebrahim and Johanna Sotiris at the Rockefeller Evelyn Gruss Lipper Cryo-Electron Microscopy Resource Center and Zhiheng Yu, Chuan Hong, and Rick Huang at the Janelia Farms Howard Hughes Medical Institute cryo-EM facility for assistance in data collection; and Sarah McCarry for editing this manuscript. We also thank the Rockefeller University and the Howard Hughes Medical Institute for financial support.

Received: October 9, 2016
Revised: October 28, 2016
Accepted: November 4, 2016
Published: December 1, 2016

REFERENCES

Adams, P.D., Afonine, P.V., Bunkóczi, G., Chen, V.B., Davis, I.W., Echols, N., Headd, J.J., Hung, L.W., Kapral, G.J., Grosse-Kunstleve, R.W., et al. (2010). PHENIX: a comprehensive Python-based system for macromolecular structure solution. Acta Crystallogr. D Biol. Crystallogr. *66*, 213–221.

Aleksandrov, L., Aleksandrov, A.A., Chang, X.B., and Riordan, J.R. (2002). The first nucleotide binding domain of cystic fibrosis transmembrane conductance regulator is a site of stable nucleotide interaction, whereas the second is a site of rapid turnover. J. Biol. Chem. *277*, 15419–15425.

Alexander, C., Ivetac, A., Liu, X., Norimatsu, Y., Serrano, J.R., Landstrom, A., Sansom, M., and Dawson, D.C. (2009). Cystic fibrosis transmembrane conductance regulator: using differential reactivity toward channel-permeant and channel-impermeant thiol-reactive probes to test a molecular model for the pore. Biochemistry *48*, 10078–10088.

Anderson, M.P., Gregory, R.J., Thompson, S., Souza, D.W., Paul, S., Mulligan, R.C., Smith, A.E., and Welsh, M.J. (1991). Demonstration that CFTR is a chloride channel by alteration of its anion selectivity. Science *253*, 202–205.

Aubin, C.N., and Linsdell, P. (2006). Positive charges at the intracellular mouth of the pore regulate anion conduction in the CFTR chloride channel. J. Gen. Physiol. *128*, 535–545.

Bagnat, M., Navis, A., Herbstreith, S., Brand-Arzamendi, K., Curado, S., Gabriel, S., Mostov, K., Huisken, J., and Stainier, D.Y. (2010). Cse1l is a negative regulator of CFTR-dependent fluid secretion. Curr. Biol. *20*, 1840–1845.

Bai, Y., Li, M., and Hwang, T.C. (2010). Dual roles of the sixth transmembrane segment of the CFTR chloride channel in gating and permeation. J. Gen. Physiol. *136*, 293–309.

Bai, Y., Li, M., and Hwang, T.C. (2011). Structural basis for the channel function of a degraded ABC transporter, CFTR (ABCC7). J. Gen. Physiol. *138*, 495–507.

Baker, N.A., Sept, D., Joseph, S., Holst, M.J., and McCammon, J.A. (2001). Electrostatics of nanosystems: application to microtubules and the ribosome. Proc. Natl. Acad. Sci. USA *98*, 10037–10041.

Baker, J.M., Hudson, R.P., Kanelis, V., Choy, W.Y., Thibodeau, P.H., Thomas, P.J., and Forman-Kay, J.D. (2007). CFTR regulatory region interacts with NBD1 predominantly via multiple transient helices. Nat. Struct. Mol. Biol. *14*, 738–745.

Basso, C., Vergani, P., Nairn, A.C., and Gadsby, D.C. (2003). Prolonged nonhydrolytic interaction of nucleotide with CFTR's NH2-terminal nucleotide binding domain and its role in channel gating. J. Gen. Physiol. *122*, 333–348.

Beck, E.J., Yang, Y., Yaemsiri, S., and Raghuram, V. (2008). Conformational changes in a pore-lining helix coupled to cystic fibrosis transmembrane conductance regulator channel gating. J. Biol. Chem. *283*, 4957–4966.

Bilan, F., Thoreau, V., Nacfer, M., Dérand, R., Norez, C., Cantereau, A., Garcia, M., Becq, F., and Kitzis, A. (2004). Syntaxin 8 impairs trafficking of cystic fibrosis transmembrane conductance regulator (CFTR) and inhibits its channel activity. J. Cell Sci. *117*, 1923–1935.

Billet, A., Mornon, J.P., Jollivet, M., Lehn, P., Callebaut, I., and Becq, F. (2013). CFTR: effect of ICL2 and ICL4 amino acids in close spatial proximity on the current properties of the channel. J. Cyst. Fibros. *12*, 737–745.

Boat, T.F., Welsh, M.J., and Beaudet, A.L. (1989). The Metabolic Basis of Inherited Disease, Sixth Edition, C.R. Scriver, A.L. Beaudet, W.S. Sly, and D. Valle, eds. (McGraw-Hill), pp. 2649–2680.

Bompadre, S.G., Sohma, Y., Li, M., and Hwang, T.C. (2007). G551D and G1349D, two CF-associated mutations in the signature sequences of CFTR, exhibit distinct gating defects. J. Gen. Physiol. *129*, 285–298.

Brown, A., Long, F., Nicholls, R.A., Toots, J., Emsley, P., and Murshudov, G. (2015). Tools for macromolecular model building and refinement into electron cryo-microscopy reconstructions. Acta Crystallogr. D Biol. Crystallogr. *71*, 136–153.

Chaves, L.A., and Gadsby, D.C. (2015). Cysteine accessibility probes timing and extent of NBD separation along the dimer interface in gating CFTR channels. J. Gen. Physiol. *145*, 261–283.

Chen, V.B., Arendall, W.B., 3rd, Headd, J.J., Keedy, D.A., Immormino, R.M., Kapral, G.J., Murray, L.W., Richardson, J.S., and Richardson, D.C. (2010). MolProbity: all-atom structure validation for macromolecular crystallography. Acta Crystallogr. D Biol. Crystallogr. *66*, 12–21.

Cheng, S.H., Gregory, R.J., Marshall, J., Paul, S., Souza, D.W., White, G.A., O'Riordan, C.R., and Smith, A.E. (1990). Defective intracellular transport and processing of CFTR is the molecular basis of most cystic fibrosis. Cell *63*, 827–834.

Cheng, S.H., Rich, D.P., Marshall, J., Gregory, R.J., Welsh, M.J., and Smith, A.E. (1991). Phosphorylation of the R domain by cAMP-dependent protein kinase regulates the CFTR chloride channel. Cell *66*, 1027–1036.

Cotten, J.F., and Welsh, M.J. (1999). Cystic fibrosis-associated mutations at arginine 347 alter the pore architecture of CFTR. Evidence for disruption of a salt bridge. J. Biol. Chem. *274*, 5429–5435.

Csanády, L., Chan, K.W., Seto-Young, D., Kopsco, D.C., Nairn, A.C., and Gadsby, D.C. (2000). Severed channels probe regulation of gating of cystic fibrosis transmembrane conductance regulator by its cytoplasmic domains. J. Gen. Physiol. *116*, 477–500.

Csanády, L., Mihályi, C., Szollosi, A., Töröcsik, B., and Vergani, P. (2013). Conformational changes in the catalytically inactive nucleotide-binding site of CFTR. J. Gen. Physiol. *142*, 61–73.

Cui, G., Zhang, Z.R., O'Brien, A.R., Song, B., and McCarty, N.A. (2008). Mutations at arginine 352 alter the pore architecture of CFTR. J. Membr. Biol. *222*, 91–106.

Dalemans, W., Barbry, P., Champigny, G., Jallat, S., Dott, K., Dreyer, D., Crystal, R.G., Pavirani, A., Lecocq, J.P., and Lazdunski, M. (1991). Altered chloride ion channel kinetics associated with the delta F508 cystic fibrosis mutation. Nature *354*, 526–528.

Davis, I.W., Leaver-Fay, A., Chen, V.B., Block, J.N., Kapral, G.J., Wang, X., Murray, L.W., Arendall, W.B., 3rd, Snoeyink, J., Richardson, J.S., and Richardson, D.C. (2007). MolProbity: all-atom contacts and structure validation for proteins and nucleic acids. Nucleic Acids Res. *35*, W375–W383.

Decaestecker, K., Decaestecker, E., Castellani, C., Jaspers, M., Cuppens, H., and De Boeck, K. (2004). Genotype/phenotype correlation of the G85E mutation in a large cohort of cystic fibrosis patients. Eur. Respir. J. *23*, 679–684.

Dolinsky, T.J., Czodrowski, P., Li, H., Nielsen, J.E., Jensen, J.H., Klebe, G., and Baker, N.A. (2007). PDB2PQR: expanding and upgrading automated preparation of biomolecular structures for molecular simulations. Nucleic Acids Res. *35*, W522–W525.

Doyle, D.A., Morais Cabral, J., Pfuetzner, R.A., Kuo, A., Gulbis, J.M., Cohen, S.L., Chait, B.T., and MacKinnon, R. (1998). The structure of the potassium channel: molecular basis of K+ conduction and selectivity. Science *280*, 69–77.

Dutzler, R., Campbell, E.B., Cadene, M., Chait, B.T., and MacKinnon, R. (2002). X-ray structure of a ClC chloride channel at 3.0 A reveals the molecular basis of anion selectivity. Nature *415*, 287–294.

El Hiani, Y., and Linsdell, P. (2010). Changes in accessibility of cytoplasmic substances to the pore associated with activation of the cystic fibrosis transmembrane conductance regulator chloride channel. J. Biol. Chem. *285*, 32126–32140.

El Hiani, Y., and Linsdell, P. (2014). Conformational changes opening and closing the CFTR chloride channel: insights from cysteine scanning mutagenesis. Biochem. Cell Biol. *92*, 481–488.

El Hiani, Y., and Linsdell, P. (2015). Functional Architecture of the Cytoplasmic Entrance to the Cystic Fibrosis Transmembrane Conductance Regulator Chloride Channel Pore. J. Biol. Chem. *290*, 15855–15865.

Elborn, J.S. (2016). Cystic fibrosis. Lancet. Published online April 29, 2016. http://dx.doi.org/10.1016/S0140-6736(16)00576-6.

Emsley, P., Lohkamp, B., Scott, W.G., and Cowtan, K. (2010). Features and development of Coot. Acta Crystallogr. D Biol. Crystallogr. *66*, 486–501.

Eyck, L.F.T. (1977). Efficient structure-factor calculation for large molecules by the fast fourier transform. Acta Crystallogr. *A33*, 486–492.

Frizzell, R.A., and Hanrahan, J.W. (2012). Physiology of epithelial chloride and fluid secretion. Cold Spring Harb. Perspect. Med. *2*, a009563.

Fu, J., Ji, H.L., Naren, A.P., and Kirk, K.L. (2001). A cluster of negative charges at the amino terminal tail of CFTR regulates ATP-dependent channel gating. J. Physiol. *536*, 459–470.

Gao, X., and Hwang, T.C. (2016). Spatial positioning of CFTR's pore-lining residues affirms an asymmetrical contribution of transmembrane segments to the anion permeation pathway. J. Gen. Physiol. *147*, 407–422.

Gao, X., Bai, Y., and Hwang, T.C. (2013). Cysteine scanning of CFTR's first transmembrane segment reveals its plausible roles in gating and permeation. Biophys. J. *104*, 786–797.

Gené, G.G., Llobet, A., Larriba, S., de Semir, D., Martínez, I., Escalada, A., Solsona, C., Casals, T., and Aran, J.M. (2008). N-terminal CFTR missense variants severely affect the behavior of the CFTR chloride channel. Hum. Mutat. *29*, 738–749.

Goehring, A., Lee, C.H., Wang, K.H., Michel, J.C., Claxton, D.P., Baconguis, I., Althoff, T., Fischer, S., Garcia, K.C., and Gouaux, E. (2014). Screening and large-scale expression of membrane proteins in mammalian cells for structural studies. Nat. Protoc. *9*, 2574–2585.

Grant, T., and Grigorieff, N. (2015). Measuring the optimal exposure for single particle cryo-EM using a 2.6 Å reconstruction of rotavirus VP6. eLife *4*, e06980.

Grigorieff, N. (2016). Frealign: An Exploratory Tool for Single-Particle Cryo-EM. Methods Enzymol. *579*, 191–226.

Guinamard, R., and Akabas, M.H. (1999). Arg352 is a major determinant of charge selectivity in the cystic fibrosis transmembrane conductance regulator chloride channel. Biochemistry *38*, 5528–5537.

He, L., Aleksandrov, A.A., Serohijos, A.W., Hegedus, T., Aleksandrov, L.A., Cui, L., Dokholyan, N.V., and Riordan, J.R. (2008). Multiple membrane-cytoplasmic domain contacts in the cystic fibrosis transmembrane conductance regulator (CFTR) mediate regulation of channel gating. J. Biol. Chem. *283*, 26383–26390.

Heymann, J.B., and Belnap, D.M. (2007). Bsoft: image processing and molecular modeling for electron microscopy. J. Struct. Biol. *157*, 3–18.

Jurkuvenaite, A., Varga, K., Nowotarski, K., Kirk, K.L., Sorscher, E.J., Li, Y., Clancy, J.P., Bebok, Z., and Collawn, J.F. (2006). Mutations in the amino terminus of the cystic fibrosis transmembrane conductance regulator enhance endocytosis. J. Biol. Chem. *281*, 3329–3334.

Kirchhofer, A., Helma, J., Schmidthals, K., Frauer, C., Cui, S., Karcher, A., Pellis, M., Muyldermans, S., Casas-Delucchi, C.S., Cardoso, M.C., et al. (2010). Modulation of protein properties in living cells using nanobodies. Nat. Struct. Mol. Biol. *17*, 133–138.

Lewis, H.A., Buchanan, S.G., Burley, S.K., Conners, K., Dickey, M., Dorwart, M., Fowler, R., Gao, X., Guggino, W.B., Hendrickson, W.A., et al. (2004). Structure of nucleotide-binding domain 1 of the cystic fibrosis transmembrane conductance regulator. EMBO J. *23*, 282–293.

Lewis, H.A., Zhao, X., Wang, C., Sauder, J.M., Rooney, I., Noland, B.W., Lorimer, D., Kearins, M.C., Conners, K., Condon, B., et al. (2005). Impact of the deltaF508 mutation in first nucleotide-binding domain of human cystic fibrosis transmembrane conductance regulator on domain folding and structure. J. Biol. Chem. *280*, 1346–1353.

Li, C., Ramjeesingh, M., Wang, W., Garami, E., Hewryk, M., Lee, D., Rommens, J.M., Galley, K., and Bear, C.E. (1996). ATPase activity of the cystic fibrosis transmembrane conductance regulator. J. Biol. Chem. *271*, 28463–28468.

Linsdell, P. (2001). Relationship between anion binding and anion permeability revealed by mutagenesis within the cystic fibrosis transmembrane conductance regulator chloride channel pore. J. Physiol. *531*, 51–66.

Linsdell, P. (2005). Location of a common inhibitor binding site in the cytoplasmic vestibule of the cystic fibrosis transmembrane conductance regulator chloride channel pore. J. Biol. Chem. *280*, 8945–8950.

Linsdell, P. (2016a). Anion conductance selectivity mechanism of the CFTR chloride channel. Biochim. Biophys. Acta *1858*, 740–747.

Linsdell, P. (2016b). Architecture and functional properties of the CFTR channel pore. Cell. Mol. Life Sci. Published online October 3, 2016. http://dx.doi.org/10.1007/s00018-016-2389-5.

Linsdell, P., Evagelidis, A., and Hanrahan, J.W. (2000). Molecular determinants of anion selectivity in the cystic fibrosis transmembrane conductance regulator chloride channel pore. Biophys. J. *78*, 2973–2982.

Locher, K.P. (2016). Mechanistic diversity in ATP-binding cassette (ABC) transporters. Nat. Struct. Mol. Biol. *23*, 487–493.

Lukacs, G.L., Chang, X.B., Bear, C., Kartner, N., Mohamed, A., Riordan, J.R., and Grinstein, S. (1993). The delta F508 mutation decreases the stability of cystic fibrosis transmembrane conductance regulator in the plasma membrane. Determination of functional half-lives on transfected cells. J. Biol. Chem. *268*, 21592–21598.

Ma, J., Zhao, J., Drumm, M.L., Xie, J., and Davis, P.B. (1997). Function of the R domain in the cystic fibrosis transmembrane conductance regulator chloride channel. J. Biol. Chem. *272*, 28133–28141.

Mastronarde, D.N. (2005). Automated electron microscope tomography using robust prediction of specimen movements. J. Struct. Biol. *152*, 36–51.

McDonough, S., Davidson, N., Lester, H.A., and McCarty, N.A. (1994). Novel pore-lining residues in CFTR that govern permeation and open-channel block. Neuron *13*, 623–634.

Murshudov, G.N., Vagin, A.A., and Dodson, E.J. (1997). Refinement of macromolecular structures by the maximum-likelihood method. Acta Crystallogr. D Biol. Crystallogr. *53*, 240–255.

Naren, A.P., Quick, M.W., Collawn, J.F., Nelson, D.J., and Kirk, K.L. (1998). Syntaxin 1A inhibits CFTR chloride channels by means of domain-specific protein-protein interactions. Proc. Natl. Acad. Sci. USA *95*, 10972–10977.

Naren, A.P., Cormet-Boyaka, E., Fu, J., Villain, M., Blalock, J.E., Quick, M.W., and Kirk, K.L. (1999). CFTR chloride channel regulation by an interdomain interaction. Science *286*, 544–548.

Navis, A., and Bagnat, M. (2015). Loss of cftr function leads to pancreatic destruction in larval zebrafish. Dev. Biol. *399*, 237–248.

Oldham, M.L., and Chen, J. (2011). Crystal structure of the maltose transporter in a pretranslocation intermediate state. Science *332*, 1202–1205.

Oldham, M.L., Davidson, A.L., and Chen, J. (2008). Structural insights into ABC transporter mechanism. Curr. Opin. Struct. Biol. *18*, 726–733.

Oldham, M.L., Hite, R.K., Steffen, A.M., Damko, E., Li, Z., Walz, T., and Chen, J. (2016). A mechanism of viral immune evasion revealed by cryo-EM analysis of the TAP transporter. Nature *529*, 537–540.

Ostedgaard, L.S., Baldursson, O., Vermeer, D.W., Welsh, M.J., and Robertson, A.D. (2000). A functional R domain from cystic fibrosis transmembrane conductance regulator is predominantly unstructured in solution. Proc. Natl. Acad. Sci. USA *97*, 5657–5662.

Perez, C., Gerber, S., Boilevin, J., Bucher, M., Darbre, T., Aebi, M., Reymond, J.L., and Locher, K.P. (2015). Structure and mechanism of an active lipid-linked oligosaccharide flippase. Nature *524*, 433–438.

Peters, K.W., Qi, J., Johnson, J.P., Watkins, S.C., and Frizzell, R.A. (2001). Role of snare proteins in CFTR and ENaC trafficking. Pflugers Arch. *443*(*Suppl 1*), S65–S69.

Pettersen, E.F., Goddard, T.D., Huang, C.C., Couch, G.S., Greenblatt, D.M., Meng, E.C., and Ferrin, T.E. (2004). UCSF Chimera–a visualization system for exploratory research and analysis. J. Comput. Chem. *25*, 1605–1612.

Prince, L.S., Peter, K., Hatton, S.R., Zaliauskiene, L., Cotlin, L.F., Clancy, J.P., Marchase, R.B., and Collawn, J.F. (1999). Efficient endocytosis of the cystic fibrosis transmembrane conductance regulator requires a tyrosine-based signal. J. Biol. Chem. *274*, 3602–3609.

Qian, F., El Hiani, Y., and Linsdell, P. (2011). Functional arrangement of the 12th transmembrane region in the CFTR chloride channel pore based on functional investigation of a cysteine-less CFTR variant. Pflugers Arch. *462*, 559–571.

Riordan, J.R. (1993). The cystic fibrosis transmembrane conductance regulator. Annu. Rev. Physiol. *55*, 609–630.

Rohou, A., and Grigorieff, N. (2015). CTFFIND4: Fast and accurate defocus estimation from electron micrographs. J. Struct. Biol. *192*, 216–221.

Rommens, J.M., Iannuzzi, M.C., Kerem, B., Drumm, M.L., Melmer, G., Dean, M., Rozmahel, R., Cole, J.L., Kennedy, D., Hidaka, N., et al. (1989). Identification of the cystic fibrosis gene: chromosome walking and jumping. Science *245*, 1059–1065.

Rubinstein, J.L., and Brubaker, M.A. (2015). Alignment of cryo-EM movies of individual particles by optimization of image translations. J. Struct. Biol. *192*, 188–195.

Scharschmidt, B.F., Keeffe, E.B., Blankenship, N.M., and Ockner, R.K. (1979). Validation of a recording spectrophotometric method for measurement of membrane-associated Mg- and NaK-ATPase activity. J. Lab. Clin. Med. *93*, 790–799.

Scheres, S.H. (2012). RELION: implementation of a Bayesian approach to cryo-EM structure determination. J. Struct. Biol. *180*, 519–530.

Seibert, F.S., Chang, X.B., Aleksandrov, A.A., Clarke, D.M., Hanrahan, J.W., and Riordan, J.R. (1999). Influence of phosphorylation by protein kinase A on CFTR at the cell surface and endoplasmic reticulum. Biochim. Biophys. Acta *1461*, 275–283.

Serohijos, A.W., Hegedus, T., Aleksandrov, A.A., He, L., Cui, L., Dokholyan, N.V., and Riordan, J.R. (2008). Phenylalanine-508 mediates a cytoplasmic-membrane domain contact in the CFTR 3D structure crucial to assembly and channel function. Proc. Natl. Acad. Sci. USA *105*, 3256–3261.

Sharma, M., Benharouga, M., Hu, W., and Lukacs, G.L. (2001). Conformational and temperature-sensitive stability defects of the delta F508 cystic fibrosis transmembrane conductance regulator in post-endoplasmic reticulum compartments. J. Biol. Chem. *276*, 8942–8950.

Smart, O.S., Neduvelil, J.G., Wang, X., Wallace, B.A., and Sansom, M.S. (1996). HOLE: a program for the analysis of the pore dimensions of ion channel structural models. J. Mol. Graph. *14*, 354–360, 376.

Smith, S.S., Steinle, E.D., Meyerhoff, M.E., and Dawson, D.C. (1999). Cystic fibrosis transmembrane conductance regulator. Physical basis for lyotropic anion selectivity patterns. J. Gen. Physiol. *114*, 799–818.

Szollosi, A., Muallem, D.R., Csanády, L., and Vergani, P. (2011). Mutant cycles at CFTR’s non-canonical ATP-binding site support little interface separation during gating. J. Gen. Physiol. *137*, 549–562.

Theodoulou, F.L., and Kerr, I.D. (2015). ABC transporter research: going strong 40 years on. Biochem. Soc. Trans. *43*, 1033–1040.

Tsai, M.F., Li, M., and Hwang, T.C. (2010). Stable ATP binding mediated by a partial NBD dimer of the CFTR chloride channel. J. Gen. Physiol. *135*, 399–414.

Van Goor, F., Yu, H., Burton, B., and Hoffman, B.J. (2014). Effect of ivacaftor on CFTR forms with missense mutations associated with defects in protein processing or function. J. Cyst. Fibros. *13*, 29–36.

Veit, G., Avramescu, R.G., Chiang, A.N., Houck, S.A., Cai, Z., Peters, K.W., Hong, J.S., Pollard, H.B., Guggino, W.B., Balch, W.E., et al. (2016). From CFTR biology toward combinatorial pharmacotherapy: expanded classification of cystic fibrosis mutations. Mol. Biol. Cell *27*, 424–433.

Vergani, P., Nairn, A.C., and Gadsby, D.C. (2003). On the mechanism of MgATP-dependent gating of CFTR Cl- channels. J. Gen. Physiol. *121*, 17–36.

Wang, W., and Linsdell, P. (2012). Relative movements of transmembrane regions at the outer mouth of the cystic fibrosis transmembrane conductance regulator channel pore during channel gating. J. Biol. Chem. *287*, 32136–32146.

Wang, W., El Hiani, Y., and Linsdell, P. (2011). Alignment of transmembrane regions in the cystic fibrosis transmembrane conductance regulator chloride channel pore. J. Gen. Physiol. *138*, 165–178.

Wang, W., El Hiani, Y., Rubaiy, H.N., and Linsdell, P. (2014a). Relative contribution of different transmembrane segments to the CFTR chloride channel pore. Pflugers Arch. *466*, 477–490.

Wang, Y., Wrennall, J.A., Cai, Z., Li, H., and Sheppard, D.N. (2014b). Understanding how cystic fibrosis mutations disrupt CFTR function: from single molecules to animal models. Int. J. Biochem. Cell Biol. *52*, 47–57.

Wang, Z., Hryc, C.F., Bammes, B., Afonine, P.V., Jakana, J., Chen, D.H., Liu, X., Baker, M.L., Kao, C., Ludtke, S.J., et al. (2014c). An atomic model of brome mosaic virus using direct electron detection and real-space optimization. Nat. Commun. *5*, 4808.

Webb, B., and Sali, A. (2014). Comparative protein structure modeling using Modeller. Curr. Protoc. Bioinformatics *Chapter 5*, Unit 5.6.

Wei, S., Roessler, B.C., Icyuz, M., Chauvet, S., Tao, B., Hartman, J.L., 4th, and Kirk, K.L. (2016). Long-range coupling between the extracellular gates and the intracellular ATP binding domains of multidrug resistance protein pumps and cystic fibrosis transmembrane conductance regulator channels. FASEB J. *30*, 1247–1262.

Winter, M.C., and Welsh, M.J. (1997). Stimulation of CFTR activity by its phosphorylated R domain. Nature *389*, 294–296.

Yang, Y., Devor, D.C., Engelhardt, J.F., Ernst, S.A., Strong, T.V., Collins, F.S., Cohn, J.A., Frizzell, R.A., and Wilson, J.M. (1993). Molecular basis of defective anion transport in L cells expressing recombinant forms of CFTR. Hum. Mol. Genet. *2*, 1253–1261.

Yu, H., Burton, B., Huang, C.J., Worley, J., Cao, D., Johnson, J.P., Jr., Urrutia, A., Joubran, J., Seepersaud, S., Sussky, K., et al. (2012). Ivacaftor potentiation of multiple CFTR channels with gating mutations. J. Cyst. Fibros. *11*, 237–245.

Zhang, J., and Hwang, T.C. (2015). The fifth transmembrane segment of cystic fibrosis transmembrane conductance regulator contributes to its anion permeation pathway. Biochemistry *54*, 3839–3850.

Zhou, J.J., Li, M.S., Qi, J., and Linsdell, P. (2010). Regulation of conductance by the number of fixed positive charges in the intracellular vestibule of the CFTR chloride channel pore. J. Gen. Physiol. *135*, 229–245.

STAR★METHODS

KEY RESOURCES TABLE

REAGENT or RESOURCE	SOURCE	IDENTIFIER
Chemicals, Peptides, and Recombinant Proteins		
2,2-didecylpropane-1,3-bis-β-D-maltopyranoside (LMNG)	Anatrace	NG310
Cholesteryl hemisuccinate (CHS)	Anatrace	CH210
Digitonin	Sigma-Aldrich	D141
sf-900 II SFM medium	GIBCO	Cat#10902-088
Cellfectin II reagents	Invitrogen	Cat#10362-100
Freestyle 293 medium	GIBCO	Cat#12338-018
Lambda PP	NEB	Cat#P0753L
PKA	NEB	Cat#P6000L
ATP	Sigma-Aldrich	A2383
Pyruvate kinase	Roche	10128163001
Lactate dehydrogenase	Roche	10127876001
Phosphoenolpyruvate	Roche	10108294001
NADH	Roche	10107735001
Critical Commercial Assays		
CNBR-activated Sepharose beads	GE Healthcare	17-0430-01
Superose 6, 10/300 GL	GE Healthcare	17-5172-01
Deposited Data		
Coordinates of the zebrafish CFTR	This paper	PDB: 5TSI
Cryo-EM map of the zebrafish CFTR	This paper	EMDB: EMD-8461
Experimental Models: Cell Lines		
Sf9	ATCC	CRL-1711
HEK293S GnTI-	ATCC	CRL-3022
Recombinant DNA		
Codon-optimized zebrafish *CFTR* in pUC57 vector	BioBasic	N/A
Zebrafish *CFTR* cloned onto a modified pEG Bacmam vector suitable for expression in mammalian cells	This paper	N/A
Sequence-Based Reagents		
Primer: Forward: ACCGCTCGAGCCACCATGCAGCGCTCTCCCGTG	IDT	N/A
Primer: Reverse: ACCGGAATTCGACAGGCGGGTATCCTGGATGTTG	IDT	N/A
Software and Algorithms		
Seriel EM	Mastronarde, 2005	http://bio3d.colorado.edu/SerialEM
Unblur	Grant and Grigorieff, 2015	http://grigoriefflab.janelia.org/unblur
CTFFIND4	Rohou and Grigorieff, 2015	http://grigoriefflab.janelia.org/ctffind4
RELION 1.4	Scheres, 2012	http://www2.mrc-lmb.cam.ac.uk/relion
alignparts_lmbfgs	Rubinstein and Brubaker, 2015	https://sites.google.com/site/rubinsteingroup/direct-detector-align_lmbfgs
FREALIGN	Grigorieff, 2016	http://grigoriefflab.janelia.org/frealign
COOT	Emsley et al., 2010	https://www2.mrc-lmb.cam.ac.uk/personal/pemsley/coot

(*Continued on next page*)

Continued

REAGENT or RESOURCE	SOURCE	IDENTIFIER
Modeler	Webb and Sali, 2014	https://salilab.org/modeller
PHENIX	Adams et al., 2010	https://www.phenix-online.org
Sfall	Eyck, 1977	http://www.ccp4.ac.uk/html/sfall.html
Refmac	Brown et al., 2015; Murshudov et al., 1997	http://www.ccp4.ac.uk/html/refmac5.html
Blocres	Heymann and Belnap, 2007	https://lsbr.niams.nih.gov/bsoft/programs/blocres.html
MolProbity	Chen et al., 2010; Davis et al., 2007	http://molprobity.biochem.duke.edu
Chimera	Pettersen et al., 2004	https://www.cgl.ucsf.edu/chimera
Pymol	PyMOL	http://www.pymol.org
APBS	Baker et al., 2001; Dolinsky et al., 2007	http://www.poissonboltzmann.org
HOLE	Smart et al., 1996	http://www.holeprogram.org
Other		
R1.2/1.3 400 mesh Au holey carbon grids	Quantifoil	1210627

CONTACT FOR REAGENT AND RESOURCE SHARING

Further information and requests for reagents may be directed and will be fulfilled by the Lead Contact Jue Chen (juechen@rockefeller.edu).

EXPERIMENTAL MODEL AND SUBJECT DETAILS

Cell Culture

Sf9 cells were cultured in sf-900 II SFM medium (GIBCO) plus 5% FBS at 27°C. HEK293S GnTI$^-$ suspension cells were cultured in Freestyle 293 medium (GIBCO) supplemented with 2% FBS at 37°C with 8% CO_2 and 80% humidity.

METHOD DETAILS

Protein Expression and Purification

DNA encoding zebrafish *CFTR* gene was synthesized and codon-optimized for expression in mammalian cells (BioBasic) and subcloned into a BacMam expression vector (Goehring et al., 2014) with a green fluorescent protein (GFP) tag attached to the C-terminus. The resulting plasmid was transformed to DH10Bac *E. coli* cells to produce bacmid DNA. Recombinant baculoviruses were generated in Sf9 cells maintained in sf-900 II SFM medium (GIBCO) plus 5% FBS using cellfectin II reagents (Invitrogen). HEK293S GnTI$^-$ suspension cells at $3x10^6$ cells/ml in Freestyle 293 medium (GIBCO) supplemented with 2% FBS were infected with 10% P3 virus. Infected cells were incubated at 37°C for 16 h; next, the temperature was decreased to 30°C and protein expression was induced by adding 10 mM sodium butyrate for 48 hr (Goehring et al., 2014).

To purify the protein, cells were resuspended in lysis buffer (20 mM Tris-HCl pH 7.5, 2 mM $MgCl_2$, 200 mM NaCl, 20% Glycerol, and 2 mM DTT) supplemented with protease inhibitors (1 μg/ml Leupepetin, 1 μg/ml Pepstatin, 1 μg/ml Aprotonin, 100 μg/ml Trypsin inhibitor, 1 mM Benzamidine, and 1 mM PMSF) and DNase (3 μg/ml) and were dispersed with a hand-held homogenizer (Polytron PT 1200E system). Membranes were solubilized with 1% 2,2-didecylpropane-1,3-bis-β-D-maltopyranoside (LMNG) and 0.2% Cholesteryl hemisuccinate (CHS) for 1.5 hr at 4°C. The cell lysates were centrifuged at 75,000 g for 40 m and the supernatant was added to CNBR-activated Sepharose beads (GE Healthcare) coupled to a GFP nanobody (Kirchhofer et al., 2010). The beads were washed with Buffer A (20 mM Tris-HCl pH 7.5, 200 mM NaCl, 0.06% Digitonin, and 2 mM DTT) and then incubated with PreScission protease (5:1 w/w ratio) at 4°C for 3 hr to remove the C-terminal GFP tag. The protein was eluted with Buffer A, concentrated and treated with Lambda PP (NEB) (40:1 w/w ratio) at 22°C for 30 m. Further purification was carried out by gel filtration chromatography using a Superose 6 10/300 column (GE Healthcare) equilibrated with Buffer A.

ATPase Activity Assay

The ATPase activity was measured using an ATP/NADH consuming coupled method (Scharschmidt et al., 1979). Purified CFTR in Buffer B (50 mM Tris-HCl pH 8.0, 150 mM KCl, 0.06% Digitonin, 2 mM $MgCl_2$, and 2 mM DTT) was treated with PKA (NEB) or Lambda PP (NEB) followed by gel filtration chromatography to remove PKA, Lambda PP, and excess ATP. The ATPase reaction buffer consists of 0.1 μM CFTR, 60 μg/ml pyruvate kinase, 32 μg/ml lactate dehydrogenase, 4 mM phosphoenolpyruvate, 0.15 mM NADH, and different amounts of ATP/Mg^{2+}. The fluorescence of NADH was excited at 340 nm and monitored at 445 nm for 45 min using an Infinite M1000 Microplate Reader (TECAN). Reaction mixtures in the absence of CFTR were also recorded to measure the background signal. All experiments were repeated three times and data were fitted to the Michaelis–Menten equation to calculate the K_m and k_{cat} values using GraphPad Prism 6.

EM Sample Preparation and Imaging

A freshly purified protein sample at 5.5 mg/ml in Buffer A supplemented with 3 mM fluorinated Fos-Choline-8 was added to Quantifoil R1.2/1.3 400 mesh Au holey carbon grids (Quantifoil), blotted with Vitrobot Mark IV (FEI), and frozen in liquid ethane. The grids were imaged with the 300keV Titan Krios (FEI) with a Gatan K2 Summit direct electron detector (Gatan). Images were recorded using Serial EM (Mastronarde, 2005) in counting mode. A Gatan Imaging filter with a slit width of 20 eV was used to improve contrasts. Data were collected with a dose rate of 7.8 electrons per physical pixel per second. Images were recorded for 7 s exposure in 50 subframes to give a total dose of 77 electrons per $Å^2$ (1.54 electrons per $Å^2$ per subframe).

Image Processing and 3D Reconstruction

Movie frames were corrected for gain reference and binned by a factor of 2 to a pixel size of 0.84 Å. Whole frame drift correction was performed using program Unblur (Grant and Grigorieff, 2015) and the contrast transfer function (CTF) was estimated using CTFFIND4 (Rohou and Grigorieff, 2015). Approximately 5,000 particles were manually picked to generate templates for automatic particle picking in RELION (Scheres, 2012). The automatically selected particles were inspected to remove false positives, resulting in a dataset of 803,894 particles. Individual particle motion correction was performed using the program alignparts_lmbfgs (Rubinstein and Brubaker, 2015). Using the structure of the TAP transporter (Oldham et al., 2016) as the initial model, 3D classification was performed in RELION (Scheres, 2012) and the best class, comprising 40% of the particles, was refined to produce a map of 6.5 Å resolution. This map was used as the initial model for refinement in FREALIGN (Grigorieff, 2016) using all 803,894 particles and frames 3-30 of each movie. The dataset was divided into two halves. One half was used for model building and model refinement (working); the other half was used as a free set for validation. The overall resolution, estimated by comparing the FSC of the two half maps, was 3.73 Å using the 0.143 cutoff criteria (Grigorieff, 2016).

Model Building

For model building, the map calculated from the working set was sharpened with BFACTOR.EXE (written by Nikolaus Grigorieff) with a resolution limit of 3.7 Å and b-factor value of -250 $Å^2$. TMD1 and TMD2 (residues 1-391 and 841-1180) were built from de novo in COOT (Emsley et al., 2010). Because the densities for the NBDs were less well defined, we first generated homology models of zebrafish NBDs based on the crystal structures of mouse NBD1 (Lewis et al., 2004) (PDB accession code 1Q3H) and human NBD2 (PDB accession code 3GD7) using the program Modeler (Webb and Sali, 2014). These models were docked into the cryo-EM map and manually adjusted. If the densities for side chains were clear, we adjusted the model based on the map; if not, we left them as they were from modeling. The final structure included residues 1-391 of TMD1, 392-402 and 437-669 of NBD1, 841-891 and 918-1180 of TMD1, and 1203-1437 of NBD2.

Model Refinement and Validation

We used PHENIX (Adams et al., 2010) with secondary structure restraints to refine the model in real space. Structural factors were calculated from the working map using the program Sfall (Eyck, 1977) and subsequently used in Refmac (Brown et al., 2015; Murshudov et al., 1997) to refine the model in reciprocal space. The R_{work} and R_{free} values were calculated using the working and the free half-maps, respectively, with a mask containing the model plus a 2 Å margin (Brown et al., 2015). To estimate the overall resolution and the degrees of overfitting, the Fourier shell correlations (FSCs) were calculated between the two half maps, the model against the working map, the other (free) half map, and full (sum) map (Wang et al., 2014c). The cryo-EM maps were masked with a large mask, which has a volume 3.5 times of the estimated volume of the model. Local resolutions were estimated using Blocres (Heymann and Belnap, 2007). The geometries of the model were validated using MolProbity (Chen et al., 2010; Davis et al., 2007).

Figures were prepared using Chimera (Pettersen et al., 2004), Pymol (http://www.pymol.org), APBS (Baker et al., 2001; Dolinsky et al., 2007) and HOLE (Smart et al., 1996).

QUANTIFICATION AND STATISTICAL ANALYSIS

To quantify the ATPase activity, mean values and the standard errors of the mean from three independent measurements were presented. The values for K_m and the maximum ATPase activity were determined by nonlinear regression of the Michaelis-Menten equation using GraphPad Prism 6. The goodness of the fit of the data, the R square values, were 0.98 for the phosphorylated protein and 0.75 for the dephosphorylated protein. The specific ATP turnover rates were calculated assuming a molecular weight of 168 kDa for zebrafish CFTR.

The orientation distribution of the particles used in the final reconstruction was calculated using RELION (Scheres, 2012). The local resolutions were estimated using Blocres (Heymann and Belnap, 2007) with the following parameters: box size 20, verbose 5, maxresolution 2.4 Å, and cutoff 0.5. The quantification and statistical analyses for model refinement and validation were integral parts of the software and algorithms used. Specifically, the R_{work}, R_{free}, average FSC, and RMS deviations were reported by Refmac, the validations of the geometries were performed by MolProbity.

DATA AND SOFTWARE AVAILABILITY

Data Resources

The accession numbers for the data reported in this paper are PDB: 5TSI and EMD: EMD-8461. The 3D cryo-EM density map has been deposited in the Electron Microscopy Data Bank under the accession number EMD: EMD-8461. Coordinates of the zebrafish CFTR structure have been deposited in the Protein Data Bank under the accession number PDB: 5TSI.

Supplemental Figures

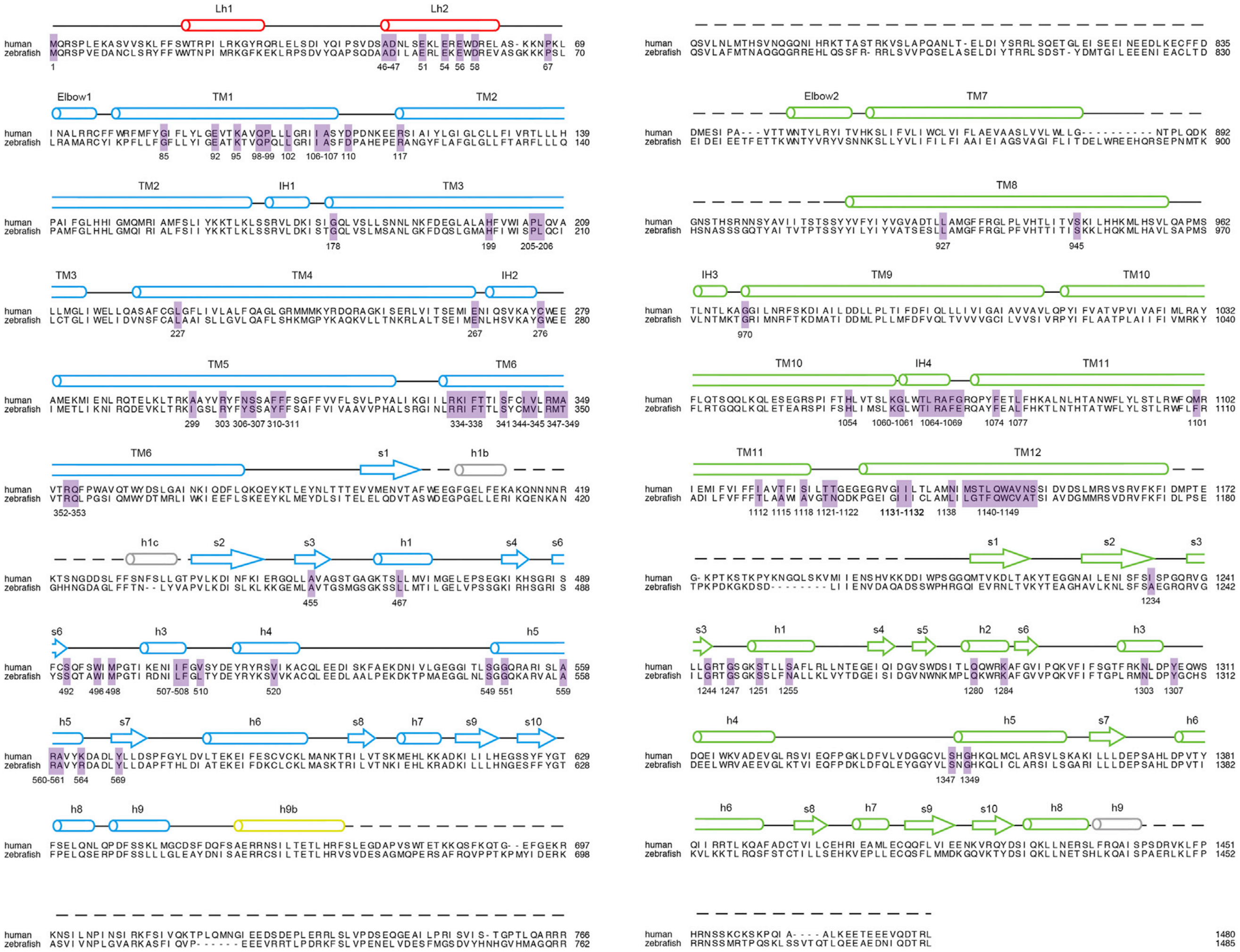

Figure S1. Sequence Alignment of CFTR from Human and Zebrafish, Related to Figures 2 and 3

Residues discussed in the paper are highlighted in purple with their positions in the human CFTR indicated.

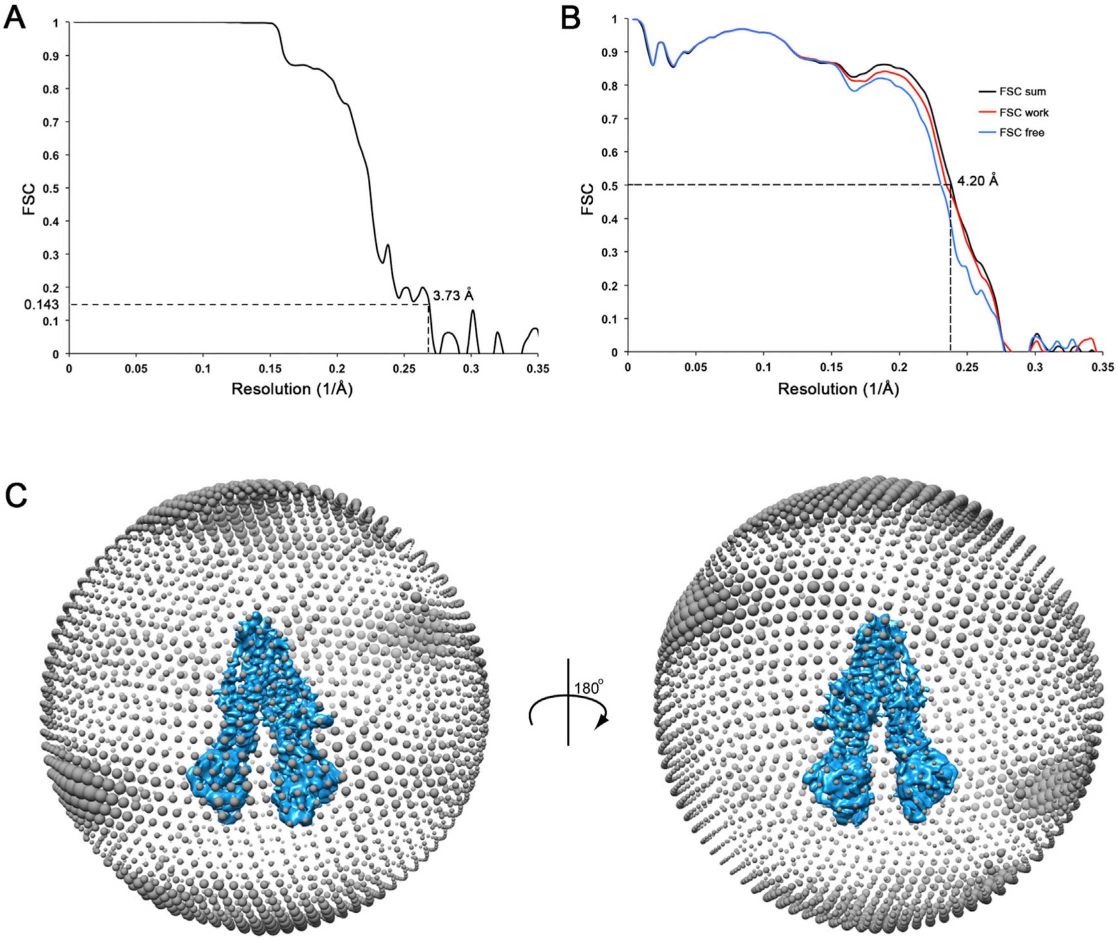

Figure S2. Data and Model Quality Assessment, Related to Figure 2

(A) A plot of the Fourier Shell Correlation (FSC) between reconstructions of two half-datasets.

(B) FSC calculated between the refined structure and the half map used for refinement (work, red), the other half map (free, blue), and the full map (black).

(C) Orientation distribution of the particles used in the final reconstruction. Each sphere indicates the number of particles from this orientation and the size of the spheres corresponds to the number of particles.

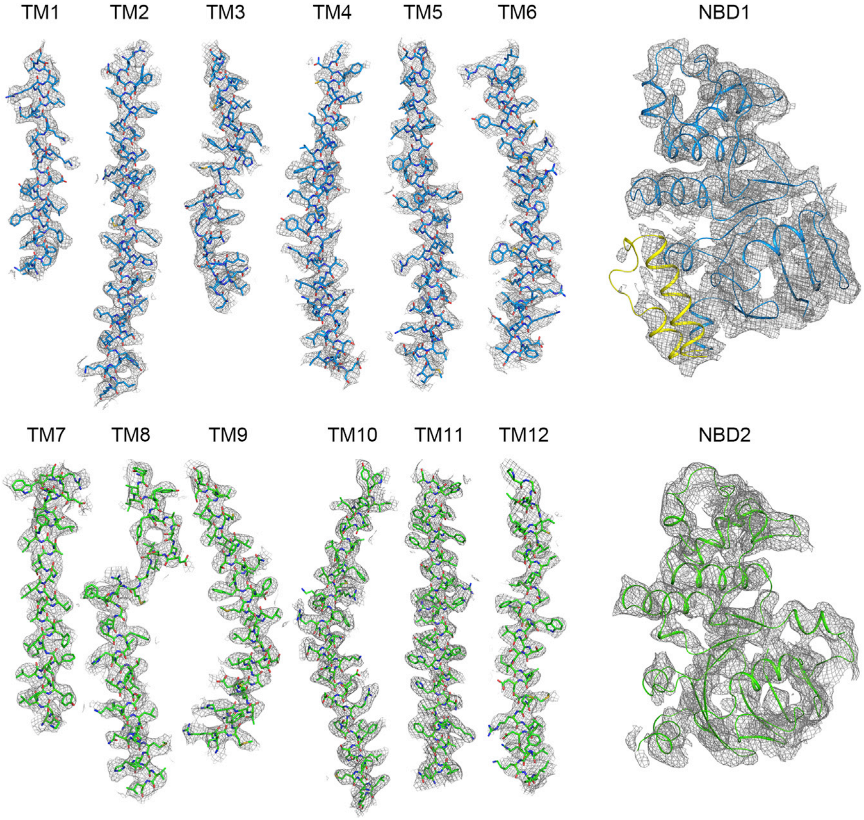

Figure S3. EM Density of Each TM Helix and the NBDs, Related to Figure 2

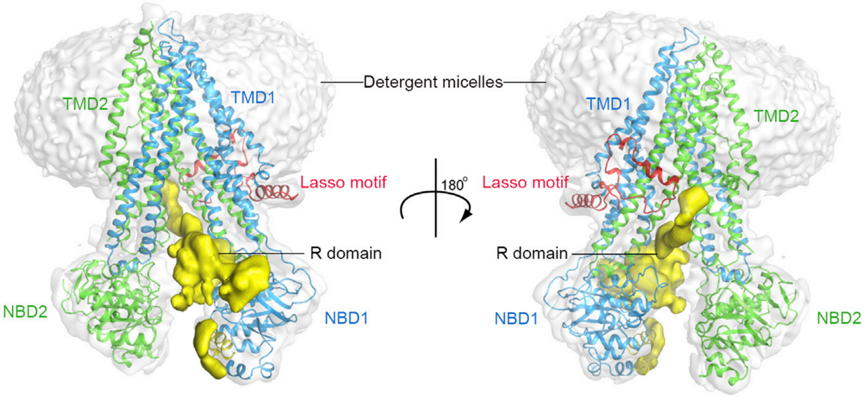

Figure S4. The Overall EM Density at a Low Contour Level to Visualize the Detergent Micelles and the R Domain, Related to Figure 3

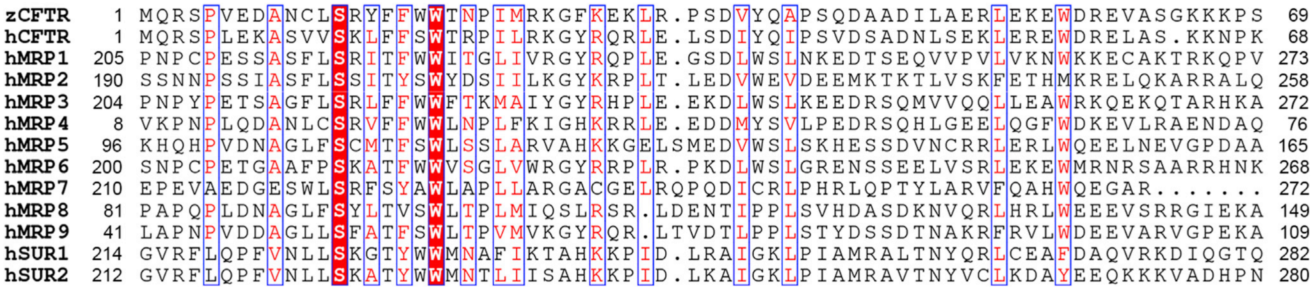

Figure S5. Sequence Alignment of the Lasso Motif among Members of the ABCC Subfamily, Related to Figure 4

Prefix “z” stands for zebrafish and “h” stands for human.